PERGAMON

Available online at www.sciencedirect.com
SCIENCE DIRECT®

International Journal of Heat and Mass Transfer 46 (2003) 2615–2627

International Journal of HEAT and MASS TRANSFER

www.elsevier.com/locate/ijhmt

Sharp-interface simulation of dendritic growth with convection: benchmarks

H.S. Udaykumar *, S. Marella, S. Krishnan

Department of Mechanical and Industrial Engineering, 4116 Seamans Center for the Engineering Arts and Science,
University of Iowa, Iowa City, IA 52242-1527, USA

Received 14 August 2002; received in revised form 12 December 2002

Abstract

We present and validate a numerical technique for computing dendritic growth of crystals from pure melts in the presence of forced convection. The Navier–Stokes equations are solved on a fixed Cartesian mesh and a mixed Eulerian–Lagrangian framework is used to treat the immersed phase boundary as a *sharp* solid–fluid interface. A conservative finite-volume discretization is employed which allows the boundary conditions to be applied exactly at the moving surface. Results are presented for a range of the growth parameters, namely crystalline anisotropy, flow Reynolds number and Prandtl number. Direct comparisons are made between the present results and those obtained with phase-field methods and excellent agreement is obtained. Values for the tip characteristics are tabulated to serve as benchmarks for computations of two-dimensional dendritic growth with convection.

1. Introduction

A method for computing the evolution of dendritic phase boundaries on fixed Cartesian grids is presented. The effect of imposed forced convection on the dendrite tip morphology is investigated. The phase front is treated as a sharp boundary that runs through the mesh and a conservative finite-volume method is applied for solution of the Navier–Stokes equations. The numerical solutions are validated against available [1–4] two-dimensional dendritic growth solutions under the effect of forced convection.

In previous work [5] we described a finite-difference technique for simulation of diffusion-controlled growth of unstable phase boundaries. For the case of dendritic solidification of pure materials from the melt, we demonstrated that a *sharp interface* approach can be developed that yields globally second-order accurate solutions to the field equations. The interface position was computed with first-order accuracy. In subsequent work [6,7], we devised a finite-volume approach for solving the incompressible Navier–Stokes equations to compute incompressible flows around fixed and moving immersed solid bodies.

This paper combines the capability to evolve dendritic phase boundaries presented in Ref. [5] with the Navier–Stokes solver in Ref. [7]. As in the case of the Navier–Stokes solutions presented in the latter reference, fluxes (of heat in the present case) are explicitly conserved across the control volume faces. Using a compact linear-quadratic interpolant [5] to evaluate the fluxes at the control volume faces that are cut by the immersed interface, a second-order accurate flux evaluation procedure is devised.

Various techniques, including phase-field [1–3,10,11], level-sets [12–14], finite-elements [15,16], and finite-difference front-tracking [5,17], have been employed to simulate dendritic solidification. The phase-field method is currently the most popular approach and was the first approach used [2,3] to determine whether the quantitative measures, such as tip radius, velocity and the selection parameter of the numerically grown dendrites could be validated against microscopic solvability theory. This method has also been used to study the behavior of dendrite tips under the influence of forced

---

* Corresponding author. Tel.: +1-319-384-0832; fax: +1-319-335-5669.
E-mail address: ush@icaen.uiowa.edu (H.S. Udaykumar).

0017-9310/03/$ - see front matter © 2003 Elsevier Science Ltd. All rights reserved.
doi:10.1016/S0017-9310(03)00038-3

convection [4]. The phase-field method falls under the class of Eulerian (i.e. fixed grid) methods called "diffuse interface" methods [18]. In such methods the interface is not a sharp phase boundary but is given a certain thickness or spread on the computational mesh. Typically, the interface thickness occupies a few mesh cells. A front-tracking method for the case of dendritic growth with convection has also been presented in [30]. However, the treatment of the solid–liquid front in the solution of the governing equations is not sharp as in the present work.

To our knowledge, the present work represents the first sharp interface simulations of dendritic growth in the presence of convection. While the interface is tracked in this work using markers and curves the approach can use other, more versatile interface representations that permit treatment of the boundaries as sharp entities, such as level-set methods [12]. This is being done in ongoing work using level-sets to track the interface. The present work places the finite-volume sharp interface approach on sound footing by directly comparing the results of the computations with results from the often used phase-field approach [4,8]. The method is shown to predict the correct physical behavior in the dendritic growth of pure materials. This validation effort augments the demonstration of grid size and orientation independence and convergence studies for the sharp interface method for dendritic growth in the diffusion-limited regime, presented in Udaykumar et al. [9]. These solutions provide benchmarks for calculations of dendrite tips growing in the presence of axially directed forced convection.

2. Solvability theory and convection effect

Microscopic solvability is the currently accepted theory for the growth of dendritic structures in solidification from the melt. Extensive reviews on the subject are available (e.g. [19]). Bouissou and Pelce [22] developed the solvability theory including convective effects on dendrites, using an Oseen flow solution under the assumptions of: (a) uniform flow at velocity U_∞ directed along an axis of the dendrite, (b) an isothermal tip and (c) the tip as a paraboloid of revolution. They obtained the solution for the translating paraboloid which provides the steady-state tip radius (ρ_t) and tip velocity (V_t) as:

$$\varDelta = Pe_t \exp(Pe_t - Pe_f) \times \int_1^\infty \frac{\{-Pe_t\eta + Pe_f\lfloor 2 + \int_1^\eta \frac{g(\varsigma)}{\sqrt{\varsigma}}\,d\varsigma - \eta\rfloor\}}{\sqrt{\eta}}\,d\eta \tag{1}$$

where $\varDelta$ is the undercooling, Pe_t the tip Peclet number $= V_t\rho_t/2\alpha$, Pe_f is the flow Peclet number $= U_\infty\rho_t/2\alpha$, Re is the Reynolds number $= (U_\infty\rho_t)/\nu = (2Pe_f)/Pr$ where α is the thermal diffusivity, ν is the kinematic viscosity and ε is the anisotropy parameter. The function $g(\zeta)$ is given by:

$$g(\varsigma) = \sqrt{\varsigma}\frac{\operatorname{erfc}(\sqrt{Re\varsigma/2})}{\operatorname{erfc}(\sqrt{Re/2})} + \frac{\sqrt{2/(\pi Re)}}{\operatorname{erfc}(\sqrt{Re/2})} \times [\exp(-Re/2) - \exp(-Re\varsigma/2)]$$

The above expressions reduce to the Ivantsov solution [20] for the no-flow case. The primary result from the solvability theory with convection is that the selection parameter for the case with flow (σ^*) is related to the value in the absence of flow ($\sigma_0^* = (2\alpha d_0)/(\rho_t^2 Vt)$), through:

$$\frac{\sigma_0^*}{\sigma^*} \cong 1 + b\chi^{11/14} \quad \text{for } \chi \gg 1,$$

while

$$\frac{\sigma_0^*}{\sigma^*} \cong 1 \quad \text{for } \chi \ll 1 \tag{2}$$

where the capillary length $d_0 = (\gamma_0 T_m C_p)/L^2$, and the parameters $\chi = (a(Re)d_0U_\infty)/(\beta^{3/4}\rho_t V_t)$, $\beta = 15\varepsilon$ and $a(Re) = \sqrt{2Re/\pi}\exp(-Re/2)\operatorname{erfc}\sqrt{Re/2}$. In the present case the Reynolds numbers are low, so that the $\chi \ll 1$ situation holds. In this limit the selection parameter should change little from the no-flow case.

3. Governing equations

To test the numerics, we grow a dendritic front for specified control parameters, namely the undercooling ($\varDelta$), capillary length (d_0), anisotropy strength (ϵ) and imposed flow strength measured by the non-dimensional velocity $U_\infty d_0/\alpha_l$. The predicted selection parameter (σ^*) and selected tip radius (ρ_t) and velocity (V_t) are then compared with the results of solvability theory and with the diffuse-interface results obtained from phase-field method [4,8]. The following non-dimensional quantities are used: length $x = X/d_0$, time $\tau = t\alpha_l/d_0^2$, velocity $\vec{u} = (\vec{U}d_0)/\alpha_l$, and temperature $\Theta = (T - T_m)/(L/C_p)$.

The incompressible Navier–Stokes equations are solved:

$$\nabla \cdot \vec{u} = 0 \tag{3}$$

$$\frac{\partial \vec{u}}{\partial \tau} + \vec{u} \cdot \nabla\vec{u} = -\nabla p + Pr\nabla^2\vec{u} \tag{4}$$

Pr is the Prandtl number $= \nu_l/\alpha_l$ where ν is the kinematic viscosity, subscript 1 stands for the liquid phase. The heat conduction equation is solved in the solid and liquid phases separately, in non-dimensional form:

$$\frac{\partial \Theta}{\partial \tau} + \vec{u} \cdot \nabla\Theta = \alpha_{l/s}^* \nabla^2\Theta \tag{5}$$

In the above the convective term applies in the solid phase, the variable $\alpha_{l/s}^* = \alpha_{l/s}/\alpha_l$ is the non-dimensional diffusivity only, and subscript l/s indicates the phase (liquid or solid). The interface temperature equation is written in non-dimensional form:

$$\Theta_i = -\mathrm{d}(\theta)\kappa \tag{6}$$

where κ is the interfacial curvature and the capillarity parameter is prescribed using the model [13] and

$$\mathrm{d}(\theta) = d_0(1 - 15\varepsilon\cos 4\theta) \tag{7}$$

For phase change of pure materials the normal velocity at a point on the front is provided by the rate of transport of latent heat away from the solid–liquid interface (Stefan condition). In non-dimensional form, this equation is:

$$V_i = \left(\left(\frac{\partial\Theta}{\partial n}\right)_{\mathrm{s}} - \left(\frac{\partial\Theta}{\partial n}\right)_{\mathrm{l}}\right) \tag{8}$$

where subscripts s and l apply to solid and liquid respectively and n represents the direction normal to the interface. Note that the boundary conditions at the farfield (at large distance r from the origin) for a crystal growing in the undercooled melt with a uniform flow directed toward the dendrite tip then become:

$$\Theta(r \to \infty, \tau) = -\Delta \tag{9a}$$

$$u(r \to \infty, \tau) = \frac{U_\infty d_0}{\alpha_{\mathrm{l}}} \tag{9b}$$

4. Numerical method

4.1. Interface tracking

The interface is tracked using markers connected by piecewise quadratic curves parametrized with respect to the arclength. Details regarding interface representation, evaluation of derivatives along the interface to obtain normals, curvatures etc. have been presented in previous papers [5,7] and are not repeated here. Also described in earlier papers are details regarding the interaction of the interfaces with the underlying fixed Cartesian mesh. These include obtaining locations where the interface cuts the mesh, identifying phases in which the cell centers lie, and procedures for obtaining a consistent mosaic of control volumes in the cells [6].

4.2. Flow solver

The fractional step scheme [24] is used for advancing the fluid flow solution in time. The Navier–Stokes equations are discretized on the Cartesian mesh using a cell-centered collocated (non-staggered) arrangement of the primitive variables $(\vec{u}, p)$. The integral forms of the non-dimensionalized governing equations are used as the starting point:

$$\oint \vec{u}\cdot\vec{n}\,\mathrm{d}S = 0 \tag{10}$$

$$\frac{\partial}{\partial\tau}\int \vec{u}\,\mathrm{d}V + \oint \vec{u}(\vec{u}\cdot\hat{n})\,\mathrm{d}S = -\oint p\vec{n}\,\mathrm{d}S + Pr\oint \nabla\vec{u}\cdot\hat{n}\,\mathrm{d}S \tag{11}$$

where $\vec{n}$ is a unit vector normal to the face of the control volume. The above equations are to be solved with $\vec{u}(\vec{x},t) = \vec{u}_\partial(\vec{x},t)$ on the boundary of the flow domain where $\vec{u}_\partial(\vec{x},t)$ is the prescribed boundary velocity, including that at the solid–liquid interface. A second-order accurate, two-step fractional step method is used [6]. A second-order Adams-Bashforth scheme is employed for the convective terms and the diffusion terms are discretized using an implicit Crank-Nicolson scheme. In addition to the cell-center velocities, which are denoted by $\vec{u}$, we also introduce face-center velocities $\vec{u}_{\mathrm{f}}$. In a manner similar to a fully-staggered arrangement, only the component normal to the cell-face is computed and stored. The face-center velocity is used for computing the volume flux from each cell in the finite-volume discretization scheme. The advantage of separately computing the face-center velocities has been discussed in the context of the current method in [6]. The semi-discrete form of the advection-diffusion equation for each cell can therefore be written as follows:

$$\int_v \frac{\vec{u}^* - \vec{u}^n}{\delta\tau}\,\mathrm{d}V = -\frac{1}{2}\oint[3\vec{u}^n(\vec{u}_{\mathrm{f}}^n\cdot\vec{n}) - \vec{u}^{n-1}(\vec{u}_{\mathrm{f}}^{n-1}\cdot\vec{n})]\,\mathrm{d}S + \frac{Pr}{2}\oint(\nabla\vec{u}^n + \nabla\vec{u}^*)\cdot\hat{n}\,\mathrm{d}S \tag{12}$$

where $\vec{u}^*$ is the intermediate cell-center velocity. The advection-diffusion step is followed by the pressure-correction step:

$$\int_v \frac{\vec{u}^{n+1} - \vec{u}^n}{\delta t}\,\mathrm{d}V = -\int_v \nabla p^{n+1}\,\mathrm{d}V \tag{13}$$

By requiring a divergence-free velocity field at the end of the time-step we get the equation for pressure,

$$\oint \nabla p^{n+1}\,\mathrm{d}S = \frac{1}{\delta t}\oint \vec{u}_{\mathrm{f}}^*\cdot\vec{n}\,\mathrm{d}S \tag{14}$$

which is the weak form of the pressure Poisson equation. Once the pressure is obtained by solving this equation, both the cell-center and face-center velocities, $\vec{u}$ and $\vec{u}_{\mathrm{f}}$ are updated separately as follows:

$$\vec{u}^{n+1} = \vec{u}^* - \delta t(\nabla p^{n+1})_{\mathrm{cc}} \tag{15}$$

$$\vec{u}_{\mathrm{f}}^{n+1} = \vec{u}_{\mathrm{f}}^* - \delta t(\nabla p^{n+1})_{\mathrm{fc}} \tag{16}$$

where subscripts cc and fc indicate evaluation at the cell center and face center locations respectively.

The energy equation, is written in semi-discrete form as:

$$\int_v \frac{\Theta^{n+1}-\Theta^n}{\delta t}\,\mathrm{d}V = -\frac{1}{2}\oint[3\Theta^n(\vec{u}_\mathrm{f}^n\cdot\vec{n})-\Theta^{n-1}(\vec{u}_\mathrm{f}^{n-1}\cdot\vec{n})]\,\mathrm{d}S + \frac{\alpha_{1/\mathrm{s}}}{2}\oint(\nabla\Theta^{n+1}+\nabla\Theta^n)\cdot\hat{n}\,\mathrm{d}S \qquad (17)$$

The above Crank–Nicolson scheme provides nominal second-order temporal accuracy.

In discrete form Eq. (17) is written, for a control volume in the Cartesian mesh indexed (i,j) as:

$$\frac{\Delta V_{ij}}{\delta t}(\Theta_{ij}^{n+1}-\Theta_{ij}^n) = \frac{\alpha_{1/\mathrm{s}}}{2}\sum_{f=1}^{5}\left(\frac{\partial\Theta^{n+1}}{\partial n}+\frac{\partial\Theta^n}{\partial n}\right)_f\Delta S_\mathrm{f} - \frac{1}{2}\sum_{f=1}^{5}[3\Theta^n(\vec{u}_\mathrm{f}^n\cdot\vec{n}) - \Theta^{n-1}(\vec{u}_\mathrm{f}^{n-1}\cdot\vec{n})]\Delta S_\mathrm{f} \qquad (18)$$

The fluxes at control volume faces are evaluated by constructing a compact two-dimensional polynomial interpolating function [6] from available neighboring cell-center values, which gives a second-order accurate approximation of the fluxes and gradients on the faces of the trapezoidal boundary cells. This interpolation scheme coupled with the finite-volume formulation guarantees that the accuracy and conservation property of the underlying algorithm is retained even in the presence of arbitrary-shaped immersed boundaries.

The discrete equations are solved using the standard line-SOR procedure, with alternate sweeps in the i- and j-directions and a standard Thomas algorithm for the solution of the resulting tri-diagonal matrix. The use of a Cartesian grid allows for the use of these fast solution procedures. The discretization of the fluid velocity and pressure Poisson equations has been described in detail in previous papers [7]. A multigrid method is used for fast solution of the pressure Poisson equation.

4.3. Computing the interface velocity

The interface velocity is obtained as described in [5]. The temperature gradient in each phase is obtained by the normal probe technique, where a normal from the interface marker is extended into each phase. The temperature values at two nodes on the normal, placed at distances equal to the local mesh spacing δx, are obtained from the background mesh by bilinear interpolation. Second-order accuracy of this technique has been demonstrated in Udaykumar et al. [5]. The gradient is then obtained as:

$$\frac{\partial\Theta}{\partial n} = \frac{4\Theta_{n1}-\Theta_{n2}-3\Theta_{\mathrm{int}}}{2\delta x} \qquad (19)$$

where subscripts $n1$ and $n2$ imply evaluations of temperature at the two nodes on the normal probe and subscript int implies the value on the interface. Having calculated the temperature gradients in each phase using Eq. (19), the interface velocities are computed at the markers using Eq. (8). These are then advected to new positions in order to evolve the interface in time.

4.4. Overall solution procedure

For curvature-driven growth problems, stability of the interface update requires an implicit coupled procedure for obtaining the field solution [26,27] and the interface position simultaneously at time level t^{n+1}. In the absence of an implicit, coupled treatment of the field solution and interface evolution, the calculations can become very stiff. The stability restriction on an explicit scheme can be very severe ($\delta t = \mathrm{O}(\mathrm{d}x^3)$) as demonstrated by Hou et al. [26]. However, solving for the fluid flow equations, particularly the pressure Poisson equation iteratively over each time step would be computationally taxing. Moreover, the interface shape couples directly with the temperature field through the Stefan and Gibbs–Thomson condition and only indirectly to the fluid flowfield through its effect on the thermal field. Therefore, within a time step we only couple the temperature field and interface update in an iterative fashion while updating the velocity and pressure fields in the usual manner outside the iteration loop.

An implicit procedure similar to that employed in [5] is used. The overall solution procedure with boundary motion is as follows:

(0) Advance to next time step $t = t + \delta t$. Iteration counter $k = 0$.
(1) Update the interface position. Determine the intersection of the immersed boundary with the Cartesian mesh. Using this information, reshape the boundary cells.
(2) Solve the fluid flow and pressure Poisson equations. Correct the velocity field to satisfy zero-divergence.
(3) Augment iteration counter, $k = k + 1$.
(4) Determine the intersection of the immersed boundary with the Cartesian mesh. Using this information, reshape the boundary cells. For each reshaped boundary cell, compute and store the coefficients appearing in discrete form for the energy equation, Eq. (18).
(5) Advance the discretized heat equation in time to obtain Θ_{ij}^k.
(6) Advance the interface position in time.
(7) Check whether the temperature field and interface have converged.
Convergence is declared if: $\max|\Theta_{ij}^k - \Theta_{ij}^{k-1}| < \varepsilon_\mathrm{T}$ and $\max|X_{ip}^k - X_{ip}^{k-1}| < \varepsilon_\mathrm{I}$, where k is the iteration number and ϵ is a convergence tolerance set to 10^{-5} in the calculations so that the solution obtained is independent of the convergence criterion.

(8) If not converged, go to step 3 for next iteration. If converged, go to step 0 for next time step.

Typically, less that five iterations of the heat equation and interface update are required for convergence since the previous time step solution provides an excellent guess to the solution at the current step. Note that with this implicit iterative approach stable computations of interface evolution can be performed with time-step sizes that are controlled by a CFL-type criterion of the form $\delta t = \lambda \delta x / \max(V_{\text{interface}}, U_{\text{flow}})$, where λ is set to 0.1 in the calculations performed.

4.5. Computational setup

The numerical method described above is now used in computations of dendritic growth and is shown to provide physically correct solutions for dendritic growth of crystals. It will be shown that the effects of all the control parameters, namely undercooling (Δ), anisotropy (ε) and imposed flow strength ($U_\infty d_0/\alpha_l$) are correctly captured by the algorithm. The results are compared quantitatively with results from the phase-field approach and qualitatively with the solvability theory.

To start the computations, a semi-circular seed crystal is placed at the origin of the computational domain of dimension $(0.5H) \times (H)$. Symmetry across the y-axis is exploited to solve in the half-space. In calculations below, we adopt $H = 2000$. The initial radius of the seed is 15 non-dimensional units (i.e. 15 capillary lengths in dimensional terms) and it is placed with its center at (0,1000). A uniform fine mesh is placed in an inner region, as shown in Fig. 1, while the mesh is coarsened linearly from the edge of the fine mesh region to the end of the domain. We have shown in earlier work [5], that the sharp interface approach gives solutions for dendritic growth that are independent of the mesh spacing and mesh orientation. In the following we compare the results of solutions that were deemed grid independent by performing a series of calculations on progressively refined grids for the case shown in Fig. 2, until the steady-state results on two successive grid sizes were found to agree adequately with each other (to within a few percent for the tip radius and velocity).

The computations are performed starting from an initial condition supplied to be $\Theta = 0$ in the solid seed and $\Theta = -\Delta$, the nondimensional undercooling value, elsewhere in the domain. Since this initial temperature field is discontinuous at the interface, the interface velocity in the initial stage of the calculations will be very large. To avoid problems with stability due to the large value of velocity, the seed is held in place (i.e. interface velocity is set to zero) for the first hundred time steps of the calculation. This allows a thermal boundary layer of the extent of a few mesh spacings to form around the seed. Thereafter the seed is allowed to grow with the velocity computed from Eq. (8). Although these initial conditions are somewhat arbitrary, the evolution of the dendrite to the desired theoretical tip shape appears to proceed regardless of the initial condition, providing a strong indication that the tip selection mechanism operates early in the growth of the dendrite. Computations are carried out until the tip velocity, radius and selection parameter have each hit steady-state values. The time required to achieve steady-state depends on the parameters assigned for each case and a typical trend is shown in Fig. 3(a) for the case with $\Delta = 0.55$, $d_0 = 0.5$ and $\epsilon = 0.03$. The non-dimensional tip velocity, $V_t d_0/\alpha_l$, tip radius ρ_t and selection parameter σ^* are shown in the figure with appropriate multipliers to fit all the curves on

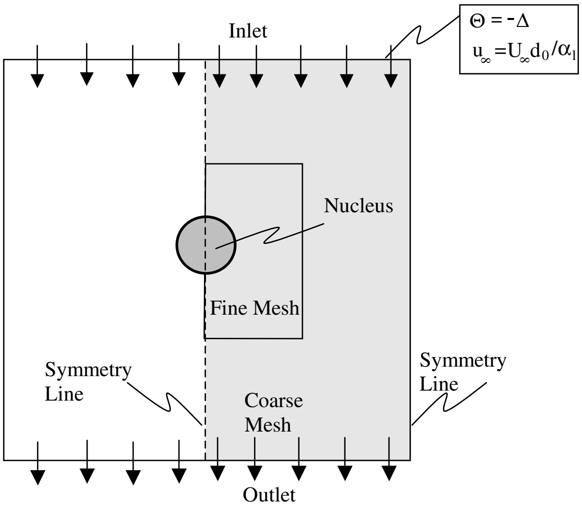

Fig. 1. Illustration of the computational set-up for the simulation of dendritic growth with flow.

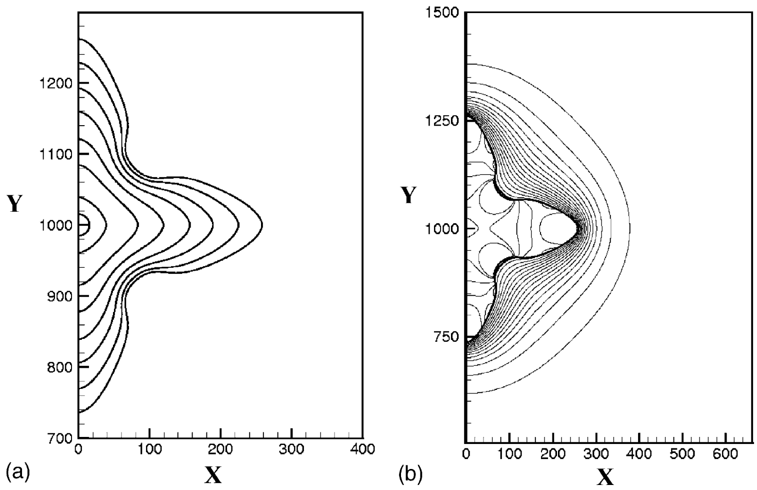

Fig. 2. Dendrite solutions for the case without flow, $\Delta = 0.55$, $\varepsilon = 0.03$. (a) Dendrite shape evolution with time. (b) Temperature contours around the dendrite for the final shape in (a).

the same plot. The selection parameter appears to be established very quickly in the growth process. The velocity and tip curvature then adjust in time until they approach steady-state values. This was found to be an interesting common aspect in the computations of dendritic growth for the range of parameters explored in this study. It appears that the pattern selection mechanism that determines σ^* operates in the entire growth process, even in the earlier stages of the growth, while the radius and velocity of the tip are "driven" towards appropriate values to yield the established σ^*. These observations are consistent with those of Plapp and Karma [29].

5. Results

The dendritic solidification calculations using the current approach has been validated against solvability theory in a previous paper [9]. Issues such as order of accuracy have been addressed in the context of solidification in Udaykumar et al. [5] and for the Navier–Stokes equations for stationary and moving boundaries in Ye et al. [6] and Udaykumar et al. [7] respectively. In this paper, we compare our results with those from the phase-field method as presented in Tong et al. [4]. Tong et al. [4] and Tong [8] in turn have shown that their results are in agreement with predictions of morphological solvability theory under certain assumptions which we will point out later in this section.

In Fig. 2 we show the dendritic growth computed in a half-space for purely diffusive transport. This case corresponds to $\Delta = 0.55$, $\varepsilon = 0.03$, $m = 4$, i.e. four-fold anisotropy. In the following calculations we maintain the capillarity parameter $d_0 = 0.5$. The y-axis is a symmetry line. Only a part of the domain is shown. Grid refinement studies were performed to ensure that the result shown is independent of grid resolution.

The tip characteristics for this case were shown to agree with solvability theory in Udaykumar et al. [9]. In Fig. 2(a) we show successive shapes of the evolving dendrite until steady-state dendrite growth is reached. Fig. 2(b) shows the isotherms in the solid and liquid phases. The contours in the solid represent the effects of interface curvature since, in the absence of temperature variations on the interface arising from the Gibbs–Thomson effect, the temperature in the solid would have been uniformly equal to the melting temperature (i.e. $\Theta = 0$).

Fig. 3 shows the effect of convection on dendritic growth for $\Delta = 0.55$, $\varepsilon = 0.03$, $m = 4$. These are the same parameters as for Fig. 2. In the case of Fig. 3 however, a flowfield is imposed. The non-dimensional flow strength at the farfield $u_\infty = 0.0675$. Fig. 3(a) shows the behavior of the tip with time. The tip velocity, radius and selection parameter are all shown in Fig. 3(a), with appropriate multipliers to clarify the plot. The tip of interest is the one facing the oncoming flow. The tip characteristics quickly approach steady-state values. Towards the end of the time duration for which this dendrite tip was computed, the tip is approaching the edge of the fine mesh region and hence the tip characteristics begin to deviate slightly from the steady-state values. The dendrite shapes at different instants in the approach to steady-state are plotted in Fig. 3(b). The temperature contours are shown in Fig. 3(c). Note that, in contrast to the shapes and temperature fields in Fig. 2, in this case convection introduces a fore-aft asymmetry. The tip facing the oncoming flow grows much faster than the one downstream due to the thinner thermal

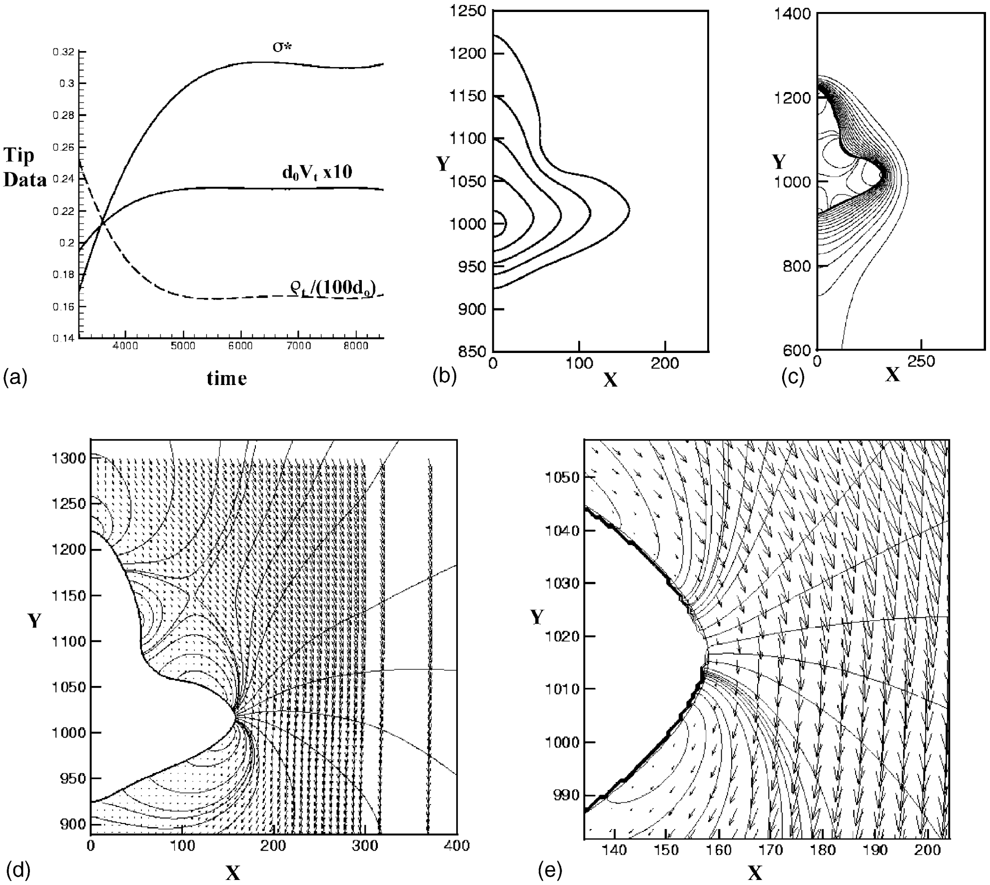

Fig. 3. Dendrite solutions for forced flow with $U_\infty = 0.0675$, $\varepsilon = 0.03$, $\Delta = 0.55$. (a) The tip characteristics of the dendrite and the approach to steady-state tip behavior. (b) Evolution of the shape of the dendrite. (c) Temperature contours around the dendrite. (d) Pressure contours and velocity vectors around the dendrite. (e) Close-up of the pressure contours and the velocity vectors around the tip growing in the +x-direction.

boundary layer at the front of the dendrite. The tip that grows laterally also grows fairly rapidly, in fact at a rate that is close to the diffusion-driven growth velocity [4,22,25]. However this tip is asymmetric across the tip axis since the thermal boundary layer on the upstream side is thinner than that on the downstream side. It is noticed that the tip that is downstream does not achieve a steady-state, at least for the duration of the computations shown. Therefore the most natural choice for comparison and analysis is the upstream tip. In Fig. 3(d) and (e), we show the velocity field and pressure contours around the dendrite for the final (steady-state) shape shown in Fig. 3(b). A zoomed-in view is also shown near the tip that grows laterally. These figures show that the present sharp-interface technique computes the velocity and pressure fields around the dendrite in a smooth fashion and that the no-slip boundary condition is applied in a sharp manner thus capturing the boundary layer without smearing.

The effect of crystalline anisotropy is shown in Fig. 4. Fig. 4(a) corresponds to $\varepsilon = 0.01$ and Fig. 4(b) to $\varepsilon = 0.05$. The flow is at $u_\infty = 0.0675$, the same value as in Fig. 3. The dendrites are evolved until a steady-state upstream tip is reached. The influence of anisotropy in sharpening the tip is clearly seen in the figures. Quantitative aspects of these dendrite tips will be discussed later. In Fig. 5 we show the evolution of the tip with $\Delta = 0.55$, $\varepsilon = 0.03$, $m = 4$ and $u_\infty = 0.14$, i.e. twice the flow strength compared to the case in Fig. 4. The effect of the enhanced convection on the dendrite tip appears to be imperceptible in the shape of the dendrite. Although the thermal field shows some enhancement of the fore-aft asymmetry due to the increased strength of the flow, the differences between Figs. 3(c) and 5(b) are small. The tip characteristics are also seen (Tables 1 and 2) to change only mildly. The variation in the tip velocity and tip radius for flow strengths lower than 0.0675 is quite significant as see from Table 2 and Fig. 7. There

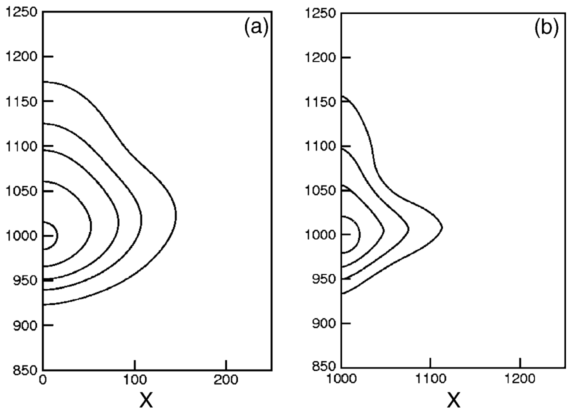

Fig. 4. Dendrite shape evolution for the case of flow with $U_\infty = 0.0675$ and $\Delta = 0.05$. (a) with $\varepsilon = 0.01$, (b) with $\varepsilon = 0.05$.

appears to be a lowering of the slopes of the V_t against u_∞ and ρ_t against U_∞ curves. This behavior has been shown in the phase-field study by Tong [8]. The tip velocity and radius appear to saturate as the u_∞ increases.

The Prandtl number in all of the above cases was 23.1, a value corresponding to the popular organic model material succinonitrile [21]. In Fig. 6 we compare the results for $Pr = 23.1$ with that for $Pr = 0.01$, this latter value being more representative of metallic melts. Fig. 6(a) shows the evolution and temperature field for $Pr = 23.1$ and $u_\infty = 0.035$, while Fig. 6(b) shows the result for $Pr = 0.01$ at the same flow strength (i.e. Reynolds number). The upstream tip for the lower Pr case grows much faster than for the higher Pr case, the steady-state velocity being about twice that of the higher Prandtl number case (Table 2). The lateral tip and the downstream tip are better developed in the higher Pr case in Fig. 6(a) when compared to the lower Pr case in Fig. 6(b). This is because the lateral and downstream tips are less affected by convection than the upstream tips. Thus, the lower Pr affects the upstream tip by increasing the tip velocity, while the other two tips are growing at essentially the same velocity as for the higher Pr case.

The interesting feature of the tip behavior is that, as can be seen in Table 2, the selection parameter is nearly independent of the Prandtl number. In the case of the lower Pr case, due to the higher diffusivity in the latter case, in the wake region, the temperature contours show greater spreading than in the higher Pr case. This spreading is more evident in Fig. 6(c) which shows the dendritic shape evolution and temperature field around the final dendritic shape for $Pr = 0.01$, $u_\infty = 0.0175$ and $\varepsilon = 0.03$, i.e. the Reynolds number is half of the value in Fig. 6(b). For this lower Re case the dendrite tip radius is larger than for the higher Re case. The wake is also broadened when compared to Fig. 6(b). Remarkably, the selection parameter, shown in Table 2 changes very little although the tip velocity and radius are changed significantly. This is entirely in agreement with theory[22,23,25] which predicts that the selection parameter is dependent on the crystalline anisotropy and only weakly on the Reynolds number, as formulated in Eqs. (1) and (2).

We now present quantitative results from the calculations where the parameters ε, Reynolds number (more specifically the flow strength u_∞) and Pr have been varied and the upstream tip characteristics have been compared with the phase-field results of Tong et al. [4]. In Fig. 7 we compare the tip velocity and tip radius for $\Delta = 0.55$, $\varepsilon = 0.03$, $m = 4$ as they vary with the imposed flow strength. As shown in the figure the results compare well with those of Tong et al. The tip velocity, in Fig. 7(a), shows slight differences at the higher flow strength but is in excellent agreement at the lower values. The tip radius, compared in Fig. 7(b) is in much better agree-

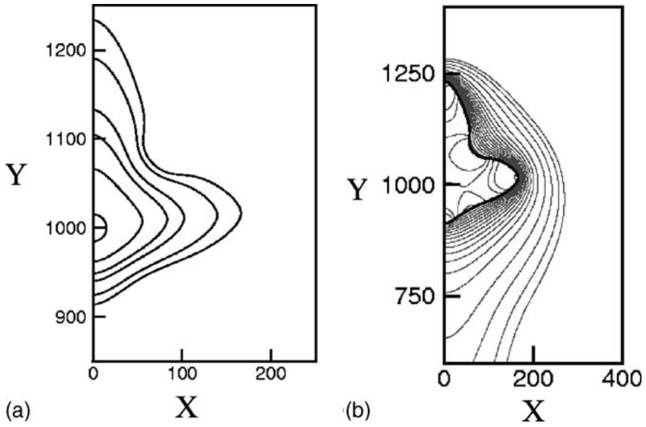

Fig. 5. Dendrite solution in the presence of flow $U_\infty = 0.14$, $\Delta = 0.55$, $\varepsilon = 0.03$. (a) The shape of the dendrite at different stages of evolution. (b) Temperature contours around the dendrite.

Table 1
Comparison of the results from the present sharp-interface calculations with phase-field results of Tong et al.

u_∞	ε	Results of	V_t^*	ρ_t^*	σ^*	Pe_t	Pe_f
0.031	0.01	Present	0.00925	102.01	0.2077	1.58	0.471
		Tong et al.	0.0085	106	0.21	1.64	0.451
0.0675	0.03	Present	0.0238	16.6	0.305	0.56	0.198
		Tong et al.	0.0231	17.7	0.28	0.59	0.205
0.0675	0.05	Present	0.031	5.47	2.22	0.185	0.084
		Tong et al.	0.029	5.7	2.15	0.193	0.071

Table 2
Tip data obtained for various parameters using the present sharp interface technique

E	Pr	u_∞	V_t^*	ρ_t^*	σ^*	Pe_t	Pe_f
0.01	23.1	0.0350	0.0100	92.20	0.0235	0.461	1.614
0.01	23.1	0.0675	0.0115	128.00	0.0106	0.736	4.320
0.02	23.1	0.0675	0.0188	30.77	0.1127	0.288	1.038
0.03	23.1	0.0175	0.0153	20.62	0.3074	0.158	0.180
0.03	23.1	0.0350	0.0190	18.20	0.3178	0.173	0.319
0.03	23.1	0.1400	0.0270	16.53	0.2711	0.194	1.157
0.05	23.1	0.0675	0.0310	5.47	2.2280	0.085	0.185
0.03	0.01	0.0050	0.0165	18.87	0.3404	0.156	0.047
0.03	0.01	0.0175	0.0270	15.43	0.3110	0.208	0.135
0.03	0.01	0.0350	0.0350	13.60	0.3089	0.238	0.238

ment for the range of flow strengths (i.e. *Re*) investigated. Fig. 8 shows the variation of the tip characteristics with the control parameters. In Fig. 8 for the case of $\Delta = 0.55$, $\varepsilon = 0.03$, $m = 4$ we plot all the tip data (by using suitable multipliers as indicated to place all the data on the same graph) against the flow strength u_∞ (or equivalently the Reynolds number). Clearly the tip velocity increases as the flow strength increases, while the tip radius decreases. The tip selection parameter remains fairly unchanged as the Reynolds number is varied. Theory, as expressed in Eq. (2), bears this observation out.

In Fig. 8(b) we compare the tip Peclet number (Pe_t) against the flow Peclet number (Pe_f) for two different anisotropy values, $\varepsilon = 0.01$ and $\varepsilon = 0.03$. For $\varepsilon = 0.03$, we compare with the data provided in Tong et al. [4]. The agreement between the present results and that in Tong et al. is excellent. In Fig. 8(c) we plot tip data against the anisotropy strength ε for a flow strength given by $u_\infty = 0.0675$. The tip velocity increases as the anisotropy increases while the tip radius decreases, i.e. the dendrite tip becomes sharper and grows faster. Notably, the selection parameter is seen to be extremely sensitive to the anisotropy strength, whereas it showed little variation with the flow strength and the Prandtl number, again in agreement with Eq. (2).

Fig. 9 shows the effects of the Prandtl number and flow strength on the upstream tip. The tip velocity in Fig. 9(a) increases with flow strength (Reynolds number) for both $Pr = 23.1$ and 0.01. However, the increase for the lower Prandtl number case is markedly higher than that for the higher *Pr*. This large difference indicates that extrapolation of observations of tip behavior obtained from model organic materials to metallic materials must be made with caution. The difference between the two Prandtl numbers is even more dramatic for the tip radius. The lower Prandtl number melts will produce much sharper dendrite tips. As an implication for solidification processing of materials, the dendrite tips in directions oriented differently with the flow are going to be much more different in growth rates as well as length scales for the lower *Pr* metallic melts than for model organic melts. It is worthy of note that the selection parameter is insensitive to the Prandtl number, at least for the limited range of parameters explored here. The selection parameter appears to decrease weakly with the Reynolds number for both Prandtl numbers. Although we have not investigated the issue of side-branching in this paper, once the tip matures noise effects will cause the tip to become unstable to side-branching [8,23]. The sharper upstream tip will likely break down first and the resulting microstructure will reflect the presence of the side branches, i.e. one would expect finer microstructures developed on the upstream side.

In the above, while we have compared our results quantitatively with the phase-field results we have only qualitatively compared the behaviors with the linearized solvability theory. The difficulty in quantitatively

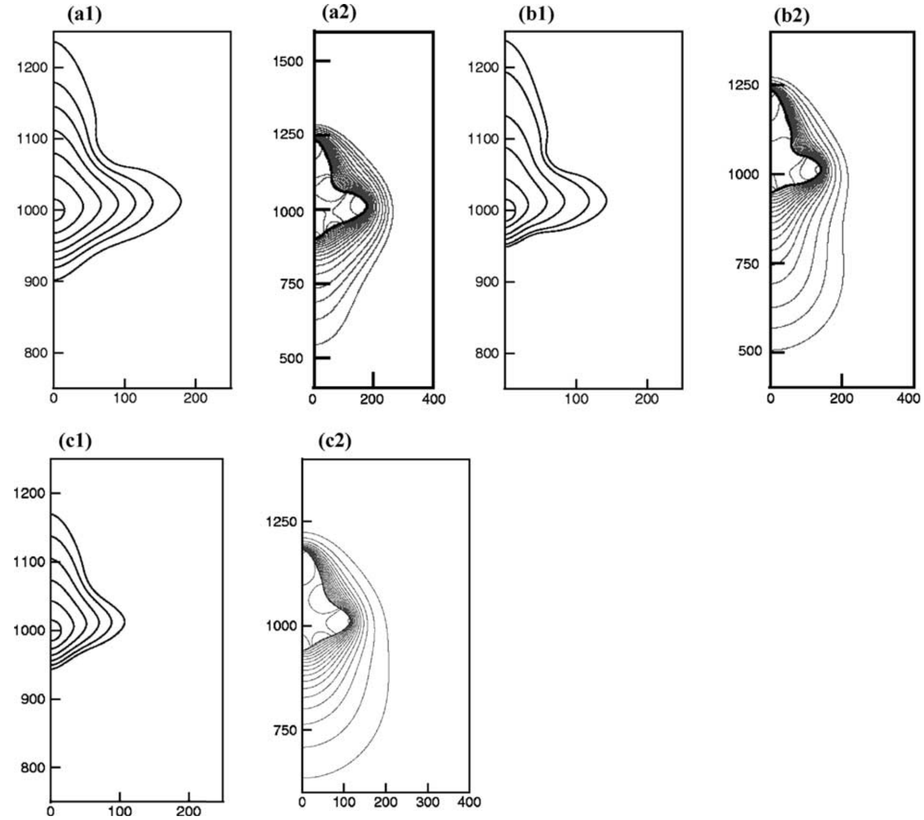

Fig. 6. Dendrite solutions with flow. Effect of Prandtl number. (a) $Pr = 23.1$, $u_\infty = 0.035$, $\varepsilon = 0.03$ (a1) shows shape evolution and (a2) shows temperature contours at final shape shown. (b) $Pr = 0.01$, $u_\infty = 0.035$, $\varepsilon = 0.03$ (b1) shows shapes and (b2) shows the temperature contours at final shape shown. (c) $Pr = 0.01$, $u_\infty = 0.0175$, $\varepsilon = 0.03$ (c1) shows the shapes and (c2) shows the temperature contours at final shape shown.

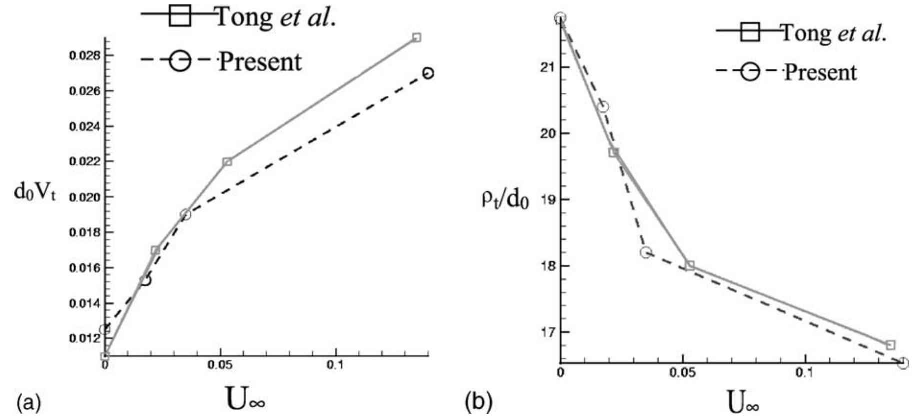

Fig. 7. Tip characteristics vs. flow strength (Reynolds number). For $\varepsilon = 0.03$, $\Delta = 0.55$. (a) The non-dimensional tip velocity vs. u_∞. (b) Non-dimensional tip radius vs. u_∞.

comparing with theory lies in the fact that the theoretical relationships for tip parameters, given by Eqs. (1) and (2) are obtained after making several simplifying assumptions. Chief among these is the assumption of a translating isothermal paraboloid of revolution. It has been shown that for large anisotropies the tip deviates

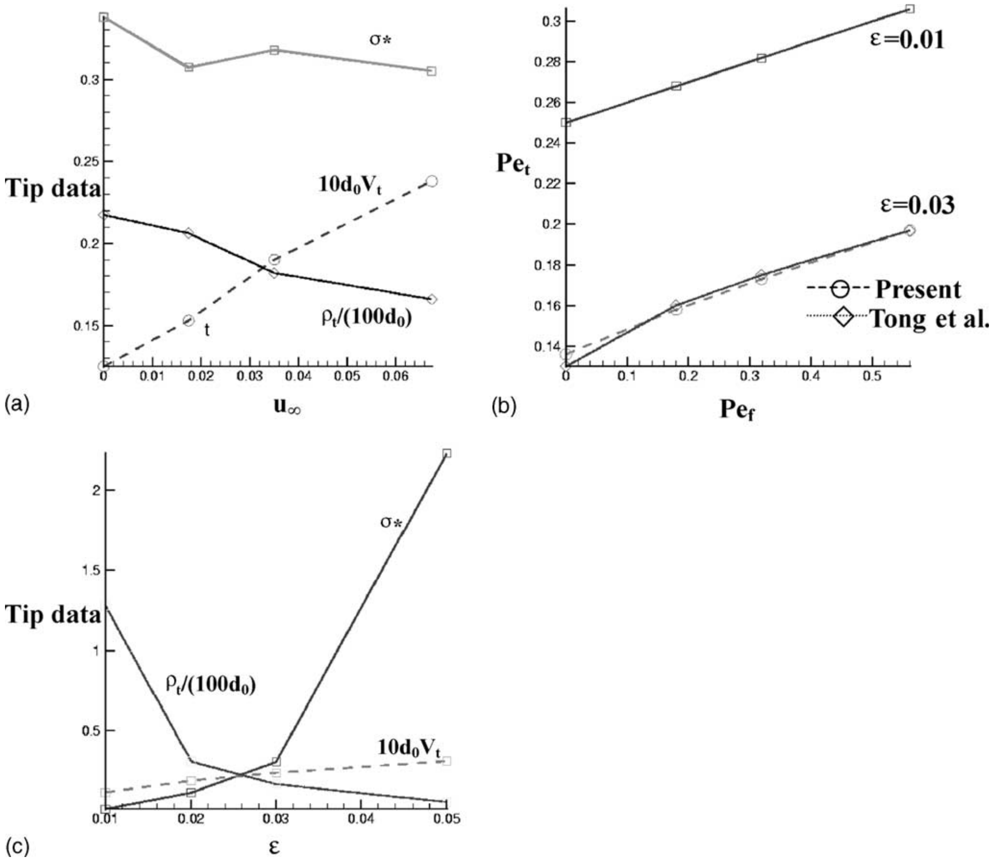

Fig. 8. Tip characteristics (radius, velocity and selection parameter) and their variation with the control and material parameters. (a) Tip data plotted against the flow strength (equivalently the Reynolds number). (b) Tip Peclet number vs Flow Peclet number for two values of anisotropy ($\varepsilon = 0.01$ and $\varepsilon = 0.03$). (c) Tip data plotted against the anisotropy strength for a flow strength of $u_\infty = 0.0675$.

significantly from a paraboloid [8]. This applied both for the diffusion-driven and forced convection influenced tip growth cases. In fact, Tong et al. [4] show that if a parabola is fit to the computed dendrite tip, then the radius of curvature of such a paraboloid at the tip in combination with the computed tip velocity gives selection parameters that are in agreement with the solvability theory. Thus, while theory is able to provide qualitative guidance as to the tip behavior and selection mechanism, quantitative comparisons are only possible when the assumption of a paraboloidal tip is made.

In Tables 1 and 2 we have tabulated results obtained for a range of parameters that may prove useful as benchmarks for the 2D simulations of dendritic growth with convection as imposed in the present calculations and Tong et al. [4]. Table 1 compares numerically our results for different Reynolds numbers and anisotropies with the available results from Tong et al. The results are shown to be numerically in excellent agreement with each other for all the tip characteristics. These results can therefore be useful as benchmarks. In Table 2 we list data on the upstream tip for a range of parameters including the two Prandtl numbers used. We also list the value of the selection parameter σ^* computed for all cases.

6. Summary

We have developed a numerical method for the computation of dendritic crystal growth where the solid–liquid interface is treated as a sharp front. Accurate solution of complicated evolving phase boundaries is facilitated by maintaining a sharp solid–liquid interface and the challenge is to develop the sharp-interface numerics on a mesh that does not conform to the interface shape. The sharp interface nature and the second-order spatial and temporal discretization coupled with a conservative finite volume scheme allows us to obtain solutions for dendritic crystal growth in good agreement with theory and with solutions of dendritic growth with flow obtained from other numerical

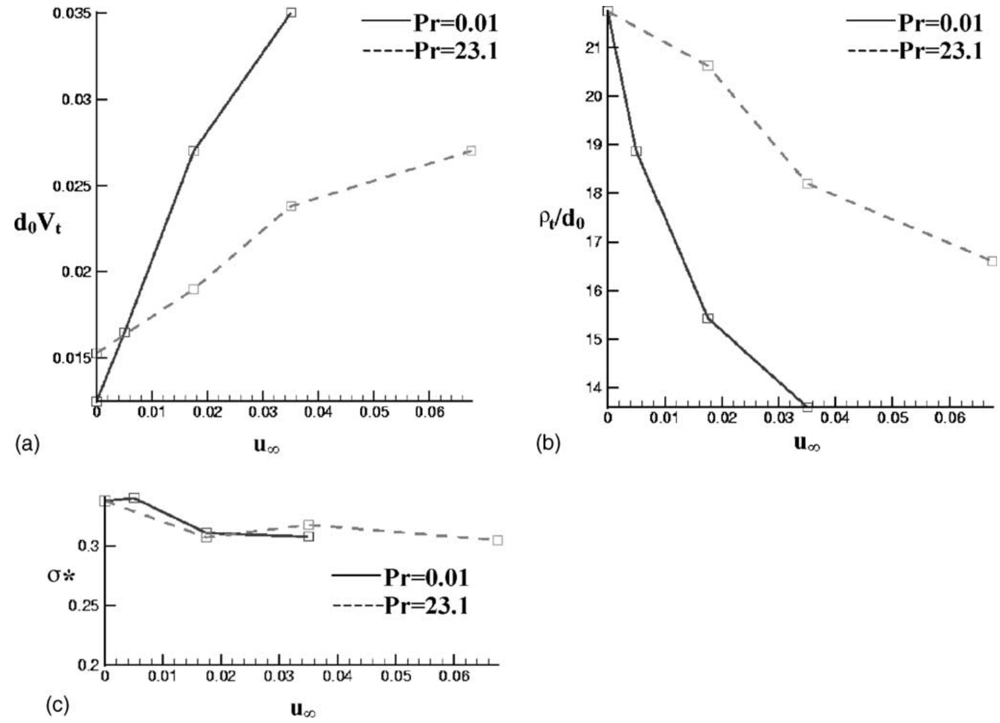

Fig. 9. Variation of the tip data with the flow strength for two different Prandtl numbers. (a) Tip velocity vs u_∞. (b) Tip radius vs u_∞. (c) Selection parameter vs u_∞.

techniques. We have demonstrated in the results presented in this paper that the effects of undercooling, anisotropy, flow strength and material property variations (such as Prandtl number) are each computed correctly by the method. The uniquely selected features of the dendrite tip, namely tip radius and tip velocity and the numerically obtained selection parameter are found to be in agreement with phase-field results. The ability of the method to treat material property jumps as discontinuous is important in the simulation of solidification in alloys and solutions, where the species transport equation comes into play. Solute segregation from the solid into the melt/solution is a critical part of such processes. The large jump in species diffusivity from solid to liquid phase is best handled by treating each phase separately, a capability that is provided by the present sharp interface technique. Ongoing work involves solution of solidification phenomena in the presence of impurities [28] and imposed flows in the presence of solutes.

Acknowledgements

This work was supported, in part, by a National Science Foundation CAREER Award (CTS-0092750) to the first author.

References

[1] G. Caginalp, P. Fife, Phase-field methods for interfacial boundaries, Phys. Rev. B 33 (1986) 7792–7794.

[2] A. Karma, W.J. Rappel, Phase-field simulation of three-dimensional dendrites: is microscopic solvability theory correct? J. Cryst. Growth 174 (1997) 54–64.

[3] A. Karma, W.J. Rappel, Phase field model of dendritic growth in two and three dimensions, Phys. Rev. E 57 (1998) 4323–4349.

[4] X. Tong, C. Beckermann, A. Karma, Velocity and shape selection of dendritic crystals in a forced flow, Phys. Rev. E 61 (2000) R49–R52.

[5] H.S. Udaykumar, R. Mittal, W. Shyy, Solid–liquid phase front computations in the sharp interface limit on fixed grids, J. Comp. Phys. 153 (1999) 535–574.

[6] T. Ye, R. Mittal, H.S. Udaykumar, W. Shyy, An accurate Cartesian grid method for viscous incompressible flows with complex immersed boundaries, J. Comp. Phys. 156 (1999) 209–240.

[7] H.S. Udaykumar, R. Mittal, P. Rampunggoon, A. Khanna, A sharp interface cartesian grid method for simulating flows with complex moving boundaries, J. Comp. Phys. 174 (2001) 1–36.

[8] X. Tong, Effects of convection on dendritic growth, PhD Thesis, University of Iowa, 1999.

[9] H.S. Udaykumar, R. Mittal, L. Mao, A finite volume sharp interface scheme for dendritic growth simulations: comparison with microscopic solvability theory, Numer. Heat Transfer B, in press.

[10] G.B. McFadden, A.A. Wheeler, R.J. Braun, S.R. Coriell, Phase-field models for anisotropic interfaces, Phys. Rev. E 48 (3) (1993) 2016–2024.

[11] Y.-T. Kim, N. Provatas, N. Goldenfeld, J. Dantzig, Universal dynamics of phase-field models for dendritic growth, Phys. Rev. E 59 (3) (1999) R2546–R2549.

[12] T.Y. Hou, Z. Li, S. Osher, H. Zhao, A hybrid method for moving interface problems with application to the Hele-Shaw flow, J. Comp. Phys. 134 (2) (1997) 236–247.

[13] Y.-T. Kim, N. Provatas, N. Goldenfeld, J. Dantzig, Computation of dendritic microstructure using a level-set method, Phys. Rev E. 62 (2) (2000) 2471–2474.

[14] N. Provatas, N. Goldenfeld, J. Dantzig, Efficient computation of dendritic microstructures using adaptive mesh refinement, Phys. Rev. Lett. 80 (15) (1998) 3308–3311.

[15] A. Schmidt, Computation of three-dimensional dendrites with finite elements, J. Comp. Phys. 125 (1996) 293–312.

[16] J.M. Sullivan, D.R. Lynch, K. O'Neill, Finite element simulations of planar instabilities during solidification of an undercooled melt, J. Comp. Phys. 69 (1987) 81–111.

[17] D. Juric, G. Tryggvasson, A front tracking method for dendritic solidification, J. Comp. Phys. 123 (1996) 127–148.

[18] D.M. Anderson, G.B. McFadden, A.A. Wheeler, Diffuse interface methods in fluid mechanics, Ann. Rev. Fluid Mech. 30 (1998) 139–165.

[19] D.A. Kessler, J. Koplik, H. Levine, Pattern selection in fingered growth phenomena, Adv. Phys. 37 (3) (1988) 255–339.

[20] G.P. Ivantsov, Temperature field around spherical, cylindrical and needle-shaped crystals which grow in supercooled melt, Doklady Akademii Nauk SSSR 58 (1947) 567–569.

[21] S.C. Huang, M.E. Glicksman, Fundamentals of dendritic solidification—I and II, Acta Metall. 29 (1981) 701–715, 717–734.

[22] Ph. Bouissou, P. Pelce, Effect of a forced flow on dendritic growth, Phys. Rev. A 40 (1989) 509–512.

[23] Ph. Bouissou, B. Perrin, P. Tabeling, Influence of an external flow on dendritic crystal growth, Phys. Rev. A 40 (1989) 509–512.

[24] Y. Zang, R.L. Street, J.R. Koseff, A non-staggered grid fractional step method for time-dependent incompressible Navier–Stokes equations in Curvilinear coordinates, J. Comp. Phys. 114 (1994) 18.

[25] Ph. Bouissou, A. Chiffaudel, B. Perrin, P. Tabeling, Dendritic side-branching forced by an external flow, Europhys. Lett. 13 (1990) 89–94.

[26] T.Y. Hou, J.S. Lowengrub, M.J. Shelley, Removing stiffness from interfacial flows with surface tension, J. Comp. Phys. 114 (1994) 312.

[27] C. Tu, C.S. Peskin, Stability and instability in the computation of flows with moving immersed boundaries: a comparison of three methods, SIAM J. Sci. Stat. Comput. 13 (1992) 1361.

[28] H.S. Udaykumar, L. Mao, Sharp interface simulation of dendritic solidification of solutions, Int. J. Heat Mass Transfer 45 (2002) 4793–4808.

[29] M. Plapp, A. Karma, Multiscale finite-difference-diffusion-Monte-Carlo method for simulating dendritic solidification, J. Comp. Phys. 165 (2000) 592–619.

[30] N. Al-Rawahi, G. Tryggvason, Numerical simulation of denritic solidification with convection: two-dimensional geometry, J. Comp. Phys. 180 (2002) 471–496.